The Astronomical Journal, 136:980–993, 2008 September doi:10.1088/0004-6256/136/3/980

COUNTER-WINDING SPIRAL STRUCTURE IN ESO 297-27

R. D. Grouchy[1,2], R. Buta[1,2], H. Salo[3], E. Laurikainen[3], and T. Speltincx[3]
[1] Department of Physics and Astronomy, University of Alabama, P.O. Box 870324, Tuscaloosa, AL 35487, USA
[2] Visiting Astronomer, Cerro Tololo Inter-American Observatory, La Serena, Chile
[3] Division of Astronomy, Department of Physical Sciences, University of Oulu, Oulu, FIN-90014, Finland
Received 2007 October 19; accepted 2008 June 14; published 2008 July 31

ABSTRACT

ESO 297-27, an intermediate-to-late-type spiral galaxy, exhibits a rare *counter-winding spiral structure* in which two sets of nonoverlapping arms open in opposite senses. We imaged ESO 297-27 along with 41 other galaxies for a survey of the measurable properties of nonbarred ringed galaxies, which is the category to which the galaxy is assigned in the Catalogue of Southern Ringed Galaxies. We analyzed broadband, narrowband, and spectroscopic data of ESO 297-27 to measure and update its physical parameters. Using a rotation curve obtained from slit spectra of the galaxy's Hα emission in combination with the Hubble–de Vaucouleurs dust asymmetry method, we determined that a single inner spiral arm is leading while at least three weak outer arms are trailing. We believe that none of the galaxy's catalogued companions are strong candidates for distorting the galaxy gravitationally. However, an unclassified companion may have perturbed ESO 297-27 in the past, but velocity data are needed to confirm this. To date, we have identified ESO 297-27 as only the second clear-cut example of a counter-winding spiral pattern, suggesting either that such patterns are very transient or that extraordinary circumstances are needed to produce them. It is important to emphasize that *counter-rotation* is not necessarily synonymous with a counter-winding spiral structure. Currently, there are no known cases of counter-rotation that show counter-winding spirals as strong as what is seen in ESO 297-27.

Key words: galaxies: kinematics and dynamics – galaxies: photometry – galaxies: spiral – galaxies: structure

1. INTRODUCTION

Spiral structure is thought to be a quasisteady density wave pattern that is maintained over many rotation periods (Lin & Shu 1964). Spiral structure may be driven in a dissipative, gaseous disk by a nonaxisymmetric perturbation such as a bar (Binney & Tremaine 1987; Schwarz 1981), or it may be a self-excited global oscillation mode, controlled by the basic state properties of the stellar and gaseous disks (Bertin et al. 1989a, 1989b). Either process results in the collection of gas and dust into localized regions. With a relatively higher density, these regions have an increased local star-formation rate, making the spiral structure stand out against the relatively dimmer disk.

An important issue that must be addressed by any spiral structure theory is the direction in which spiral arms wind within a galaxy. In order to answer this question observationally, we need two pieces of information: which side of the galaxy is moving toward the observer and which edge of the galaxy is tilted toward the observer. The former can be determined through major axis spectroscopic observations. As for the latter, the most direct approach to determining the near side of the galaxy is to use the *dust asymmetry method* described by Hubble (1943) and de Vaucouleurs (1958). If a galaxy with a thin layer of dust is imbedded in a disk with a significant bulge, then the bulge is seen through the dust layer on the near side of the disk. On the far side of the disk, the bulge is viewed in front of the dust layer. This leads to an apparent reddening or extinction asymmetry that is caused entirely by tilt. Knowledge of the near side of the disk based on this asymmetry, in conjunction with rotation data, allows the sense of winding of spiral arms to be determined. As a result of studies like this, astronomers have accepted for decades that the spiral structure observed in most, if not all, galaxies is trailing.

Building on this assumption, it is thought that multiple arms within a single galaxy unwind in the same sense, either counterclockwise or clockwise. Although both leading and trailing density waves are thought to be part of the dynamics and propagation of spiral structure, the swing amplification mechanism of Toomre (1981) demonstrates the robustness of trailing waves over leading waves. In the swing amplifier feedback cycle, trailing waves always have a larger amplitude than the leading waves from which they started (Binney & Tremaine 1987). In addition, only trailing spiral density waves transfer angular momentum outwards (Lynden-Bell & Kalnajs 1972), a process essential to maintaining the spiral (Lin & Lau 1979). Thus, leading spirals, if they do exist, would be expected to swing quickly into stronger, more obvious trailing spirals, and as a consequence, leading spirals should be very rare.

Pasha & Smirnov (1982) and Pasha (1984) revisited the question of spiral arm winding and found possible examples of leading spiral structures mostly within interacting spiral galaxies. None of these examples has been verified or survived further study (e.g., Sharp & Keel 1985), but Pasha concluded that astronomers should not take for granted the sense of winding of spirals even if leading spiral structures might be uncommon. This is because leading spirals are not absolutely ruled out by spiral structure theories.

We further challenge the assumption of trailing spiral structures in the presence of *counter-winding spirals*. These rare spirals have two sets of arms existing in different parts of the disk and appear to be opening in opposite directions. The orientation of the spiral arms to each other implies that one set of arms must be leading instead of trailing as previously assumed.

To date, the best-known example of a counter-winding spiral is the nearly face-on southern galaxy NGC 4622. Byrd et al. (1989) first noticed its unusual structure in a photograph published by Shu (1982). Interestingly, the two sets of arms are separated by a bright inner ring, and there is no trace of a bar. Inside the ring, a single spiral arm opens counterclockwise while two stronger arms unwind clockwise outside of the ring

Table 1
Observing Log for Optical Imaging of ESO 297-27

Telescope (m)	Filter name	Central wavelength (Å)	Wavelength range (Å)	Exposure (s)	Airmass	Seeing (arcsec)	Resolution (arcsec pix^{-1})
CTIO 1.5	*B*	4201	1050	600	1.022	0.57	0.434
CTIO 1.5	*V*	5475	1000	600	1.022	0.61	0.434
CTIO 1.5	*I*	8067	1485	600	1.025	0.49	0.434
CTIO 1.5	Hα	6693	75	1800	1.021	0.58	0.434
CTIO 1.5	Continuum	6477	75	1800	1.024	0.50	0.434
ESO-NTT 3.6	*B*	4223	941	600	1.053	0.87	0.363
ESO-NTT 3.6	*J*	12500	2.9	1080	1.062	0.39	0.288

(Buta et al. 1992). The counter-winding patterns are best seen in a *Hubble Space Telescope* (*HST*) *V*-band image (Buta et al. 2003) and can be made even more obvious with Fourier decomposition (Buta et al. 1992, 2003). NGC 4622 is positioned deep within a cluster, giving it many substantial companions which may be responsible for perturbing the galaxy's disk into this odd morphology. With only one clear-cut example of counter-winding spiral structures identified to date, any additional possible examples of leading spiral patterns are of great interest and should be investigated more thoroughly.

In this paper, we describe photometric and spectroscopic observations of another candidate of a counter-winding spiral, ESO 297-27. In the Catalogue of Southern Ringed Galaxies (CSRG), Buta (1995) recognized the object during a survey of ringed galaxies using the small-scale SRC-J Southern Sky Survey, and classified the galaxy as type SA(rs)b. Buta noted that the inner pseudo-ring is made of a single spiral arm winding counter to two weaker outer arms. Our observations were obtained to delineate the galaxy's structure and to verify the counter-winding components of its spiral arm pattern. Preliminary discussions of this galaxy are given by Buta et al. (2003, 2007) and Grouchy & Buta (2005).

The observations of ESO 297-27 are part of a larger project aimed at improving our understanding of nonbarred ringed galaxies. This class of normal galaxies recognized by Sandage (1961) and de Vaucouleurs (1959) is more poorly understood than its barred counterpart. As a group, nonbarred ringed spirals are rarer than the barred ringed spirals (Buta & Combes 1996), but are abundant enough to be well represented in galaxy catalogues. A preliminary look at some of our survey data is provided in the de Vaucouleurs Atlas of Galaxies (Buta et al. 2007).

2. OBSERVATIONS

2.1. Optical Data

The optical images of ESO 297-27 were obtained on two occasions. We took one set of images in 2002 August using the Cerro Tololo Inter-American Observatory (CTIO) 1.5 m telescope with a focal ratio of $f/7.5$. Attached to the telescope was a Tek 2K CCD camera with a quad amplifier, a pixel scale of 0.″434, and a gain of 1.5 e^- per ADU. These data were used for determining properties of the galaxy such as position angle, axis ratio, absolute magnitudes, and color. We took the second set of images in 2006 July with the European Southern Observatories New Technology Telescope (ESO NTT). The 3.6 m telescope gave us a *B*-band image with a pixel scale of 0.″363 and a *J*-band image with a pixel scale of 0.″288. These images, which are superior in depth and quality to the earlier CTIO 1.5 m observations, confirmed our previously calculated values.

Table 1 lists all of the optical observations of ESO 297-27. We imaged the galaxy in broadband filters equivalent to Johnson's *B*- and *V*-, Cousins *I*-, and the near-infrared Johnson *J*-band filter. We took a 75 Å wide narrowband image centered on the galaxy's redshifted Hα emission of 6702 Å. We took a second narrowband image centered on 6477 Å, which was used for subtracting the underlying continuum in the Hα filtered image.

The broadband optical images were reduced using standard IRAF[4] procedures to remove cosmic rays and instrumental effects. For the CTIO images, Graham's (1982) standards were observed each night in each filter at low, medium, and high airmasses in order to calibrate the images to the standard system. The *B*-band image from the NTT was calibrated with observations of several of Landolt's (1973, 1983) standards.

The *J*-band image was prepared using IRAF routines, following the procedure recommended by Joyce (1992). Due to the high sky brightness in this waveband, separate prechosen local sky fields were observed. Both galaxy and sky frames were dithered to eliminate bad pixels from all frames and foreground stars from the sky frames. The flat fielding was performed on different images using a lamp that illuminated a white spot in the dome. A total integration time of 1080 s was obtained. Calibration of the *J*-band image was made using Two Micron All Sky Survey (2MASS) photometry in a 14″ aperture, listed as $J = 13.72$ on the NASA/IPAC Extragalactic Database (NED) Web site.

The narrow-band images were also reduced using standard IRAF procedures to remove cosmic rays and instrumental effects. To calibrate the Hα images into standard flux units, we followed the techniques outlined in Jacoby et al. (1987) and Crocker et al. (1996). We checked the accuracy of our scale factor by applying it to planetary nebulae with known fluxes (Kohoutek & Martin 1981), which were observed each night. We found that our scale factor resulted in nebular fluxes which were too bright by 0.04 dex.

2.2. Spectroscopic Data

In 2004 June, we obtained spectroscopic data of ESO 297-27 using the R-C spectrograph and a Loral 3K CCD attached to the CTIO 4.0 m telescope. We used the KPGL #3 grating in combination with a 1.″0 slit to observe Hα gaseous emission and MgIb stellar absorption for the major and minor axes of the galaxy. Table 2 lists the spectroscopic observations taken for ESO 297-27.

The spectroscopic data were prepared using standard IRAF procedures. An arc lamp of He, Ne, and Ar was imaged for

[4] IRAF is distributed by the National Optical Astronomy Observatory, which is operated by the Association of Universities for Research in Astronomy, Inc., under cooperative agreement with the National Science Foundation.

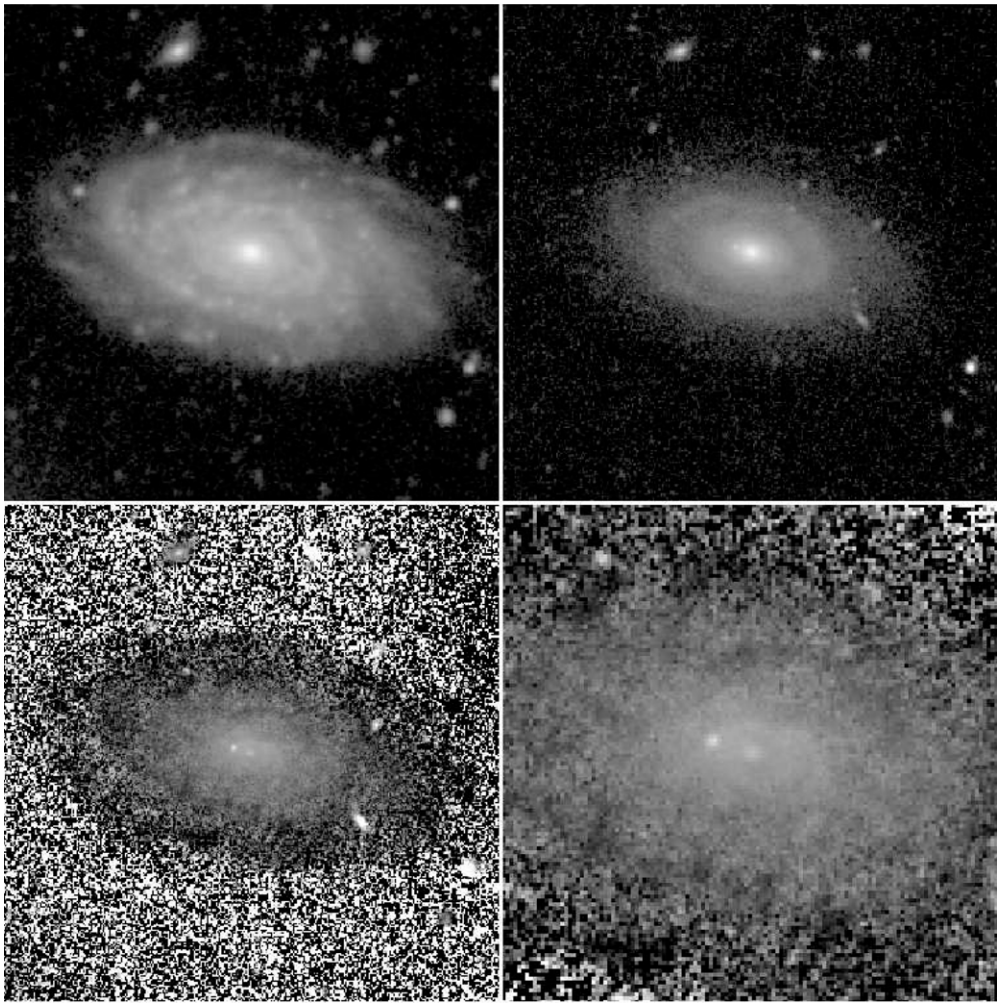

Figure 1. Upper left: B-band NTT image of ESO 297-27 showing the structure in the range of 20.4–29.0 mag arcsec^{-2}. Upper right: J-band NTT image showing the structure in the range of 17.0–26.0 mag arcsec^{-2}. Lower panels: $B - J$ color index map showing the color distribution in the range of 1.0–4.0. The field of view shown is 1.′8 × 1.′8 except for the lower right panel, which covers the inner 0.′77 × 0.′77. North is up and east is to the left.

Table 2
Observing Log for Spectroscopic Imaging of ESO 297-27

Telescope (m)	Grating (KPGL)	Axis	Airmass	Exposure (s)	Velocity dispersion (Å pix^{-1})	$\sigma_{\rm instr}$ @ 6700 Å (km s^{-1})
CTIO 4.0	#3	Major	1.281	1800	1.22	47
CTIO 4.0	#3	Minor	1.179	1200	1.22	47

wavelength calibration purposes. Due to the lengthy exposure times, we imaged the arc lamp before and after a galaxy exposure in order to interpolate any changes in wavelength calibration through time. K-giants were also observed for calibration purposes.

A 30-minute exposure resulted in an instrumental velocity dispersion of $\sigma = 47$ km s^{-1} at the wavelength of 6700 Å and a dispersion of 1.22 Å per pixel. Our spectra showed strong Hα emission throughout the galaxy except for at the center of the galaxy where the emission was relatively weak but still detectable. The [N II] emission line was strongest near the center and weaker toward the edge of the galaxy's disk. We chose a grating with a spectral range large enough to observe the MgIb stellar absorption and the Hα emission lines simultaneously. The stellar absorption line was too weak to detect due to poor weather conditions. As a result, we were unable to look for possible counter-rotation between the gas and stars of ESO 297-27.

3. MORPHOLOGY

The upper panels of Figure 1 show the NTT B- and J-band images of ESO 297-27. These are the highest quality images we obtained of this galaxy. They are displayed in units of mag arcsec^{-2} making them comparable to galaxy images shown in the de Vaucouleurs Atlas of Galaxies (Buta et al. 2007). At first glance, ESO 297-27 appears to be an entirely normal intermediate-to-late-type spiral of de Vaucouleurs revised Hubble–Sandage (VRHS) classification SA(rs)bc. Detailed inspection of the B-band image reveals that ESO 297-27 has a counter-winding spiral structure with a single inner arm opening counterclockwise and at least two faint outer arms opening clockwise (see Figure 2). The images, oriented with north pointing up and east to the left, show that the counter-winding nature of the spiral pattern is most prominent on the eastern side of the galaxy. It is here where the strongest of the three outer arms breaks away from the inner arm. Where NGC 4622 has a distinct

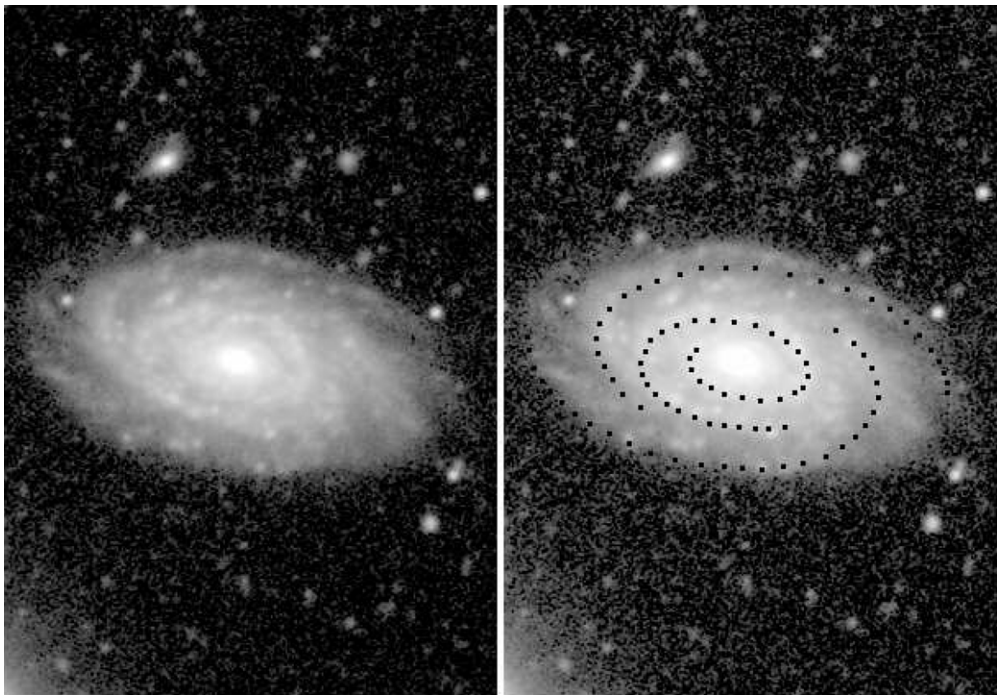

Figure 2. Both panels show the blue light image of ESO 297-27 with a field of view of 1.′8 × 2.′6. The panel on the right includes a tracing of the $m = 1$ and $m = 2$ Fourier components of the galaxy overlaid onto the image to emphasize the counter-winding structure. The inner arm appears to unwind clockwise while two outer arms appear to open counterclockwise. The unaltered image on the left is included for direct comparison.

ring separating its counter-winding structure, ESO 297-27's inner arm is a pseudo-ring separating itself from the outer arms.

The inner arm appears smooth and well defined in the ESO NTT J-band image but looks patchy and distorted in the ESO NTT B-band. It winds more than 360° around the bulge of the galaxy. In contrast, two of the outer arms extend 180° while the third extends only 100° in blue light. These outer arms are barely detectable in the J-band image. These results are verified by the CTIO *BVI* images.

The lower panels of Figure 1 show $\mu_B - \mu_J$ color index maps of ESO 297-27, coded such that red features are light and blue features are dark. These images show a clear dust asymmetry near the center that indicates the north side as the near side of the disk. This result is verified in Section 4.3.1 and is critical to our interpretation of the sense of winding of the arm patterns. The CTIO images also showed a color asymmetry indicating the north side as the near side of the galaxy. However, due to the lower resolution of the CTIO images, the color asymmetry was less certain.

Table 3
Global Characteristics of ESO 297-27

Parameter	RC3	This paper
α (J2000)	$01^h45^m10.^s8$	...
δ (J2000)	$-41°52'48''$	...
z	0.02122	...
Adopted distance		85 ± 6 Mpc (NED)
VRHS Type	SA(rs)b	SA(rs)bc (NTT)
logD$_{25}$	1.11	1.103 (NTT)
logR$_{25}$	0.24	0.254 (NTT)
ϕ_{25}	78°	77.°3 (NTT)
A_B(Gal) (mag)	0.03	0.067 (NED)
B_T	14.85	14.92 ± 0.02 (CTIO)
B_T	14.85	14.98 ± 0.03 (NTT)
B_T^o	14.45	14.51 ± 0.03
M_B^o	...	−20.1 ± 0.4
$(B-V)_T$	...	0.65 ± 0.02 (CTIO)
$(V-I)_T$	...	1.01 ± 0.03 (CTIO)
$(B-J)_T$	...	2.63 ± 0.04 (NTT)
Log $L_{H\alpha}$	...	41.3 ± 0.5 (CTIO)
SFR ($M_\odot$ yr^{-1})	...	2 ± 3 (CTIO)

4. ANALYSIS

4.1. Basic Parameters

Basic physical parameters of ESO 297-27 are available from the Third Reference Catalogue of Bright Galaxies (hereafter RC3; de Vaucouleurs et al. 1991). However, the galaxy has not been the target of any specific study. When possible, our images were used to update and improve the previously established values. RC3 parameters are listed in Table 3. The heliocentric radial velocity of ESO 297-27 is 6362 km s^{-1} (Mathewson et al. 1992). Using this value, the NED gives several estimates of the distance based on $H_o = 73 \pm 5$ km s^{-1} Mpc^{-1}. We adopted a distance of 85 ± 6 Mpc based on these estimates.

The axis ratio, q, and the position angle, PA, of ESO 297-27 were determined by fitting ellipses to the outer disk isophotes of the galaxy. We used the IRAF routine ELLIPSE to fit these isophotes for the three CTIO images and the two NTT images. The resulting mean disk axis ratios and position angles are listed in Table 4. Varying radial ranges were chosen for calculating these values. For the CTIO data, ELLIPSE fitted isophotes out to $r = 40''$ in the I band and $r = 50''$ in the B and V bands, while the NTT data were fitted out to $r = 60''$ in the B band. Even though the NTT images are deeper than the CTIO images, the isophotal axis ratios from the five different images are within 2σ of each other. Taking a weighted average of the values gives a mean axis ratio $\langle q \rangle$(CTIO) = 0.559 ± 0.001, which corresponds to an inclination of 58° if the disk is assumed to be an oblate spheroid having an intrinsic flattening of $q_o = 0.2$. The weighted average of the position angle is 81.°3, while the

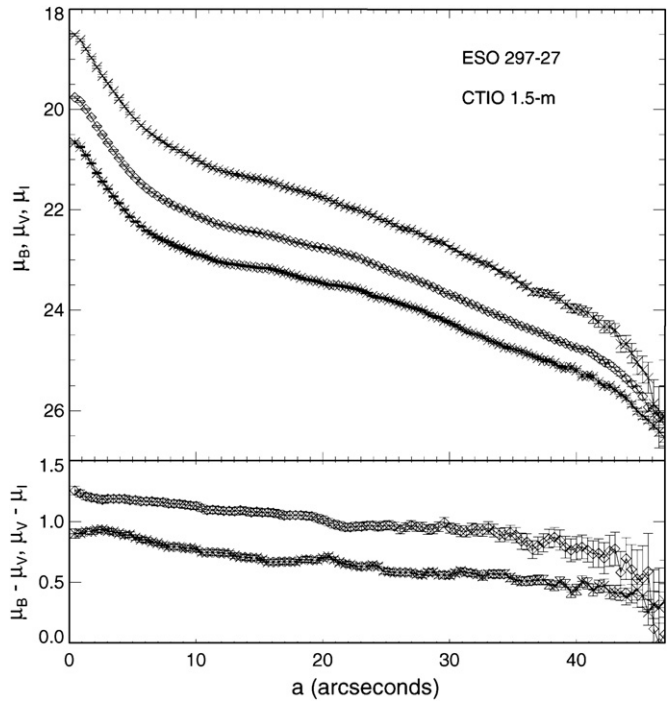

Figure 3. Upper panel: azimuthally averaged surface brightness profiles of ESO 297-27 from CTIO 1.5 m B (asterisks), V (diamonds), and I (crosses) images. Lower panel: azimuthally averaged $B-V$ (asterisks) and $V-I$ (crosses) color profiles of ESO 297-27.

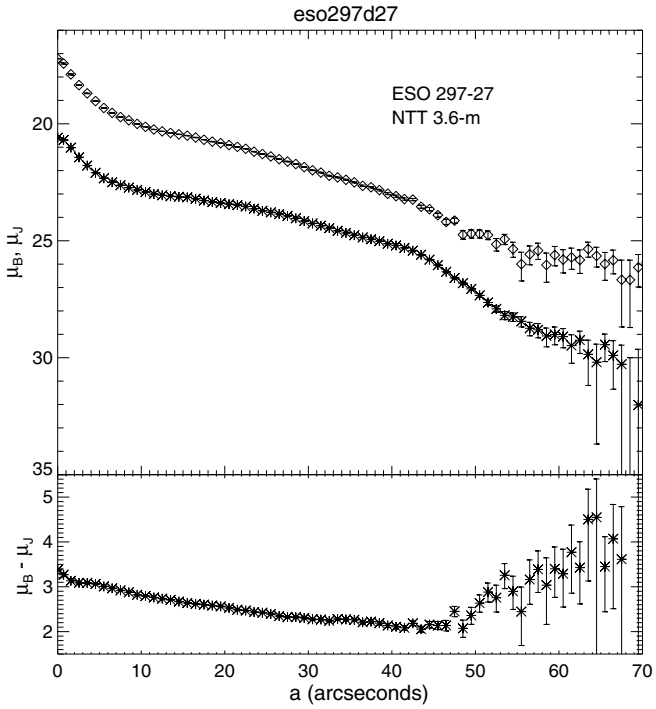

Figure 4. Azimuthally averaged surface brightness (upper panel) and color (lower panel) profiles of ESO 297-27 from NTT 3.6 m B (asterisks) and J (diamonds) images.

Table 4
Photometric Orientation Parameters of ESO 297-27

Filter	$\langle q \rangle$	$\langle \phi \rangle$
B(CTIO)	0.560 ± 0.003	81.7 ± 0.30
V(CTIO)	0.553 ± 0.002	81.9 ± 0.18
I(CTIO)	0.596 ± 0.006	78.4 ± 0.60
B(NTT)	0.562 ± 0.001	80.6 ± 0.11
J(NTT)	0.547 ± 0.003	78.6 ± 0.21
Means	0.559 ± 0.001	81.3 ± 0.13

Note. q is the minor-to-major-axis ratio of isophotes and ϕ is the position angle relative to north (J2000).

RC3 value is 78°. The latter value agrees well with our estimate of the position angle of the $\mu_B = 25.00$ mag arcsec^{-2} isophote. Our estimates of the isophotal diameter $\log D_{25} = 1.103$ and axis ratio $\log R_{25} = 0.254$ agree well with RC3 values (see Table 3). These parameters are based on our deep NTT image.

Azimuthally averaged surface brightness profiles are shown in Figures 3 and 4. All of the profiles were created using our derived values for the axis ratio and the position angle of ESO 297-27. The profiles for the NTT data extend to larger radii because of the greater depth and resolution of these images compared with the CTIO data. All of the profiles show a strong color gradient as well as a change in slope near $r = 42''$. Our profile looks similar to the ellipse-fitted profile of ESO 297-27 by Mathewson et al. (1992, their Figure 2). The NTT B-band profile especially shows what can be described as a disk cutoff similar to what is often seen in edge-on galaxies (van der Kruit & Searle 1981). At larger radii ($r = 55''$), another change in slope occurs that corresponds to a reddening in the $\mu_B - \mu_J$ color profile. This can be seen clearly only in the NTT B-band profile.

The profiles were used to calculate integrated magnitudes for ESO 297-27. For each filtered CTIO image, we used a least-squares fit, extrapolated out to infinity, and assumed an exponential decline at large radii. For the NTT data, extrapolations were not necessary, and we calculated the total magnitudes by integrating to $r = 70''$. The results are listed in Table 3. Our derived values of the total B magnitude fall within the uncertainty of $B_T = 14.90 \pm 0.09$ derived by Lauberts & Valentijn (1989).

We estimated the Hα flux emission from the narrowband Hα image of ESO 297-27 (see Figure 5). Using the axis ratio and position angle derived from the broadband images, we fitted an ellipse with a major axis radius of 80.″4 to the Hα image. Since the filter is wide enough to be contaminated with nearby [N II] emission, the flux detected within this ellipse is a measure of the Hα + [N II] emission. The Hα + [N II] flux is measured to be 1.35×10^{-13} ergs s^{-1} cm^{-2}. We scaled the flux by a factor of 0.67 to remove the [N II] contribution (Kennicutt et al. 1994; hereafter KTC). We also corrected the flux using a standard correction of 1.1 mag for internal extinction (KTC). The Galactic extinction for ESO 297-27 was calculated and corrected for using the NED value for $E(B-V)$ and the relationship $A(\lambda) = E(B-V)X(\lambda)$ (Seaton 1979), where $X(6563) = 2.46$ (Howarth 1983). Applying these corrections results in an estimated Hα luminosity of 2.29×10^{41} erg s^{-1}. Assuming solar metallicity and a Salpeter initial mass function (IMF), we converted this flux to a star-formation rate using the ratio $1\ M_\odot\ \mathrm{yr}^{-1} = 1.26 \times 10^{-41}$ erg s^{-1} (KTC). This gave a star-formation rate of 2 $M_\odot$ yr^{-1} for ESO 297-27, well within the range found for other intermediate-to-late-type spirals by Kennicutt (1983). The luminosity from Hα emission along with the galaxy's star-formation rate are listed in Table 3.

The major axis rotation profile is derived from a long slit spectrum of Hα and [N II] emission lines (see Figures 6 and 7). Each point on the plot was estimated by fitting a Gaussian to

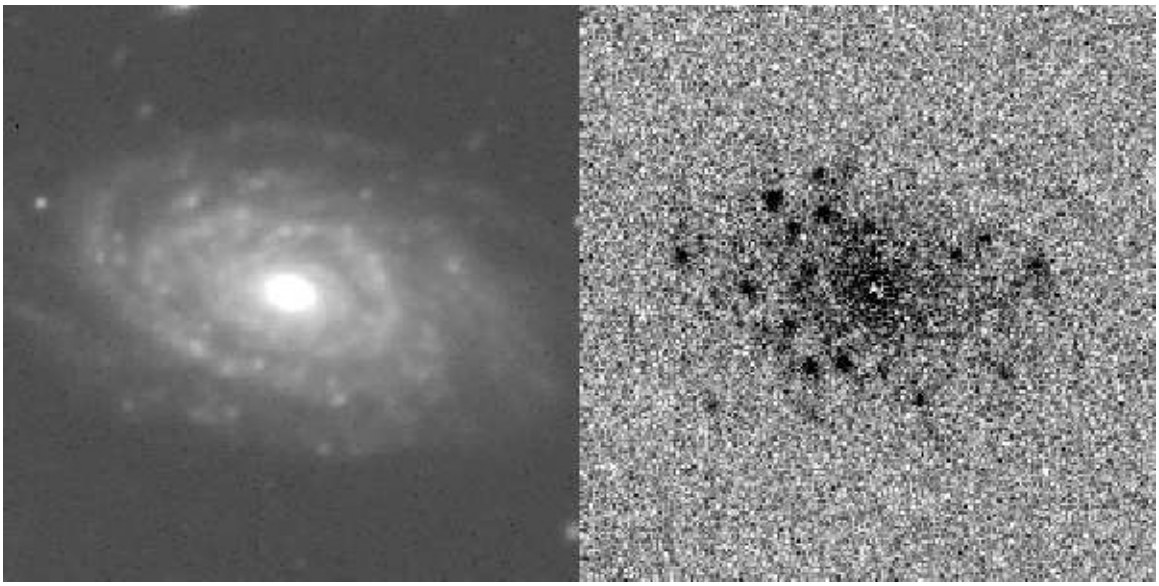

Figure 5. Left panel: blue light ESO NTT image of ESO 297-27 displayed as a positive image in which white corresponds to emission. Right panel: Hα + [N II] emission from ESO 297-27 shown as a negative image with black corresponding to emission. This image shows that ESO 297-27 has a disk of diffuse ionized gas with an incoherent pattern of H II regions. Both images are $1\farcm5 \times 1\farcm5$.

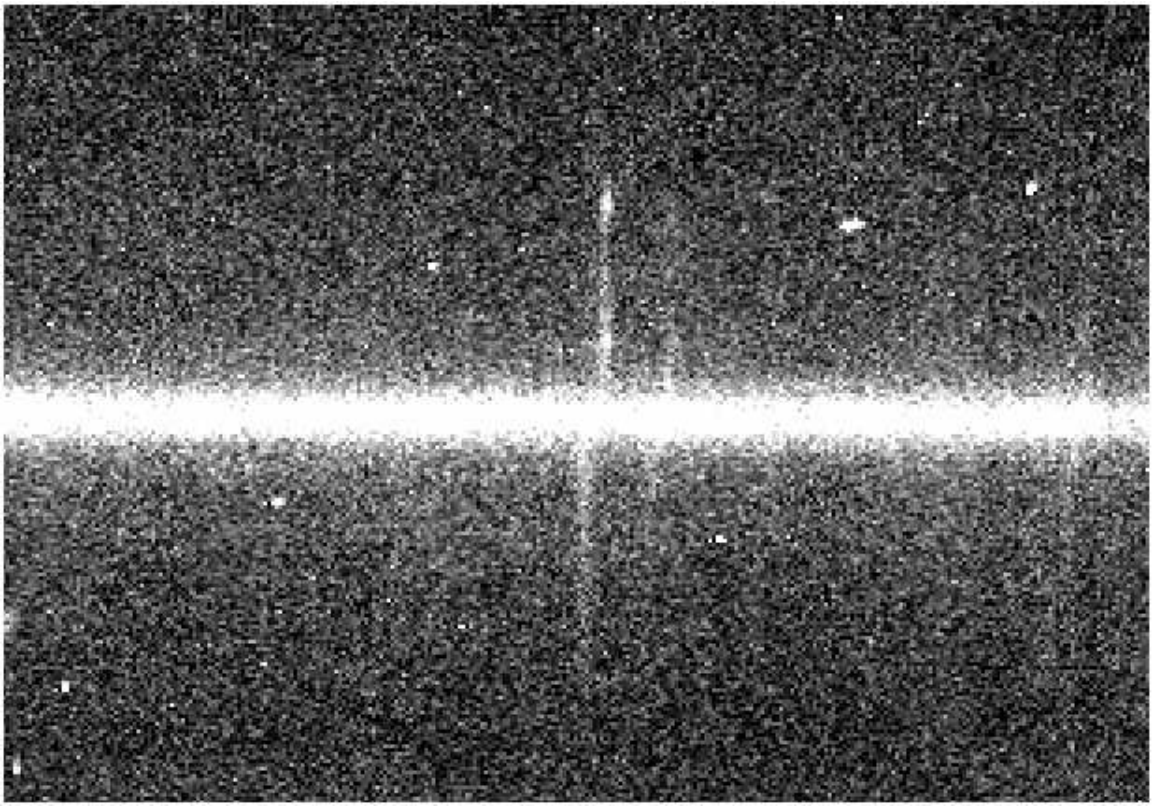

Figure 6. Long slit spectrum along the major axis of ESO 297-27 centered on the redshifted Hα emission ($\lambda \approx 6702$ Å) with [N II] emission just to the right. The positive y-direction is northeast along the major axis and wavelength increases to the right along the x-axis. The width of the image is 374.54 Å.

the emission line using the IRAF routine SPLOT. We calculated the error in Gaussian's centroid with the following intensity weighted formula developed by Keel (1996):

$$\sigma_\lambda = \frac{\sigma_{\rm cont} c \delta\lambda^{1.5}}{I \lambda d^{0.5}}, \quad (1)$$

where $\sigma_{\rm cont}$ is a noise estimate of the continuum, c is the speed of light, $\delta\lambda$ is the full width at half-maximum (FWHM) of the observed Gaussian, λ is the observed wavelength, d is the dispersion that is specific to the CCD used, and I is the intensity of the line. Using a 3σ cut-off, we rejected only two measurements, each of which had a Gaussian FWHM that was very near zero. The velocities plotted are heliocentric values, but the profile and errors are not corrected for the galaxy's tilt to the line of sight (see Figure 8 for the deprojected velocity curve). We found the [N II] emission to be stronger near the center of the

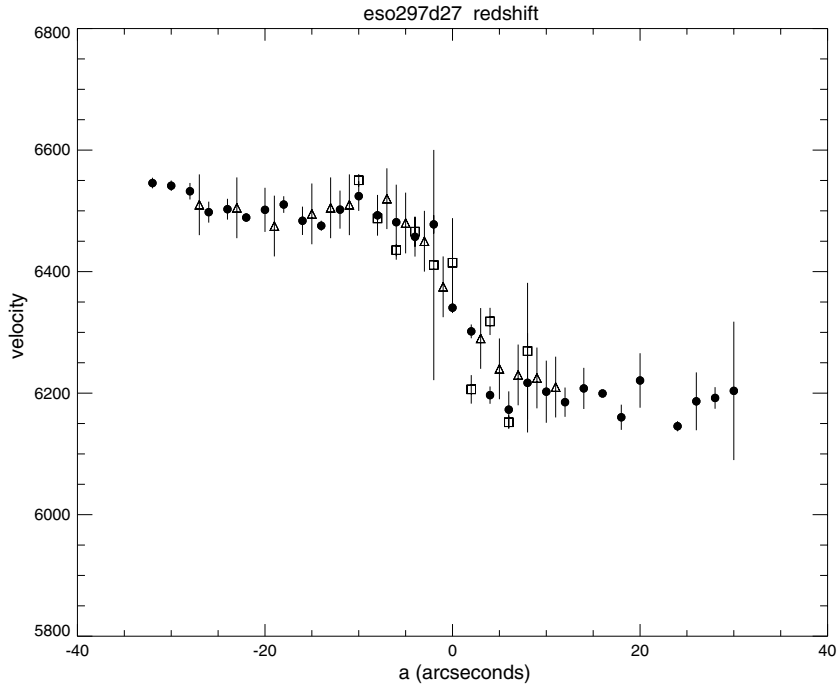

Figure 7. ESO 297-27's major axis velocity profile in the plane of the galaxy. Negative radii are in the direction northeast of the center along the major axis. Solid points are based on Hα while boxes are based on [N II] at 6583 Å. The triangles are estimated velocities from the published Mathewson et al. (1992) data. The recessional velocity is estimated to be 6365 ± 28 km s^{-1}.

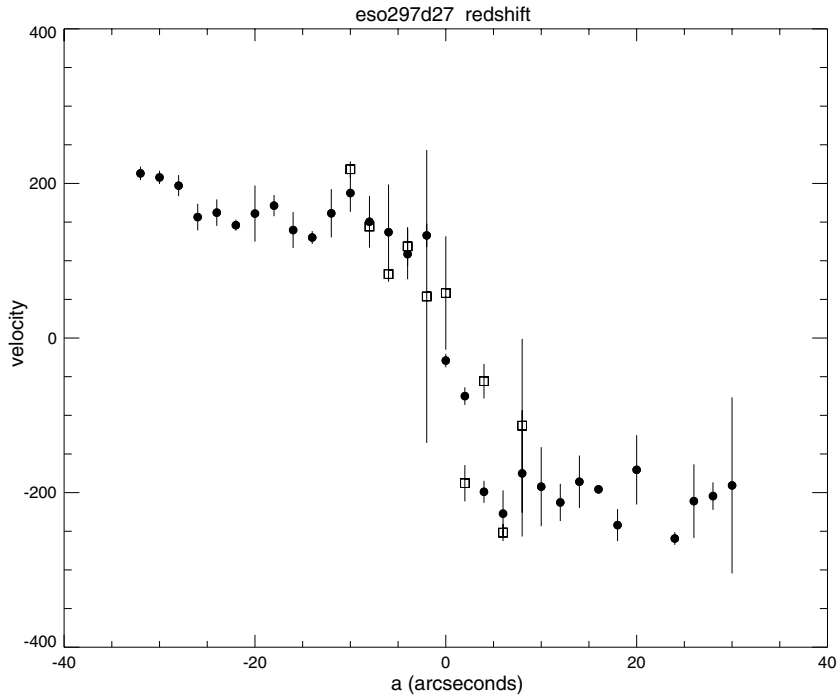

Figure 8. Deprojected rotation curve of ESO 297-27 from slit spectroscopy. Negative radii are in the direction northeast of the center along the major axis. Solid points are based on Hα while boxes are based on [N II] at 6583 Å.

galaxy and the Hα emission stronger toward the outer disk. A plot of [N II]/Hα versus radial distance can be seen in Figure 9. Rubin et al. (1997, their Figure 11) found a similar trend for intermediate-type galaxies. They found Sb galaxies to have higher [N II] flux compared with the Hα flux toward the center. This ratio eventually fell below unity for all of the galaxies; however, Rubin et al. did not find the same trend in Sc galaxies whose ratio remained below unity even in the inner disk. ESO 297-27 is an Sbc galaxy; it has a maximum [N II]/Hα ratio of 4.6, but the ratio falls below unity around $r = 4''.5$ or 2.1 kpc. Rubin et al. (1997) found the Sb galaxies NGC 4192 and NGC 4343 to have [N II]/Hα ratios that fell below unity approximately at 0.1 kpc and 0.4 kpc, respectively (their Figure 11, lower panels). The [N II]/Hα ratio being less than unity in the disk of the galaxy is expected in the presence of younger OB stars found in star-forming regions of the disk (Rubin et al. 1997).

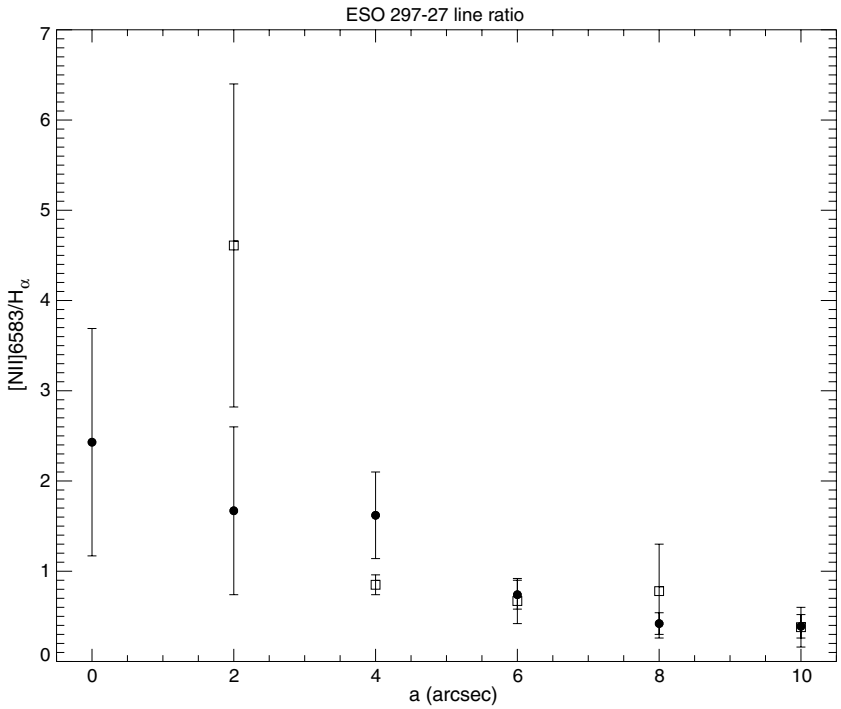

Figure 9. [N II]/Hα ratio vs. major axis radius for ESO 297-27. Squares represent negative radii (northeast) along the slit and filled circles represent positive radii (southwest) along the slit. The ratio falls below unity at approximately 4.″5 or 2 kpc, which is a marker of photoionization from young OB stars in regions with ongoing star formation (Rubin et al. 1997).

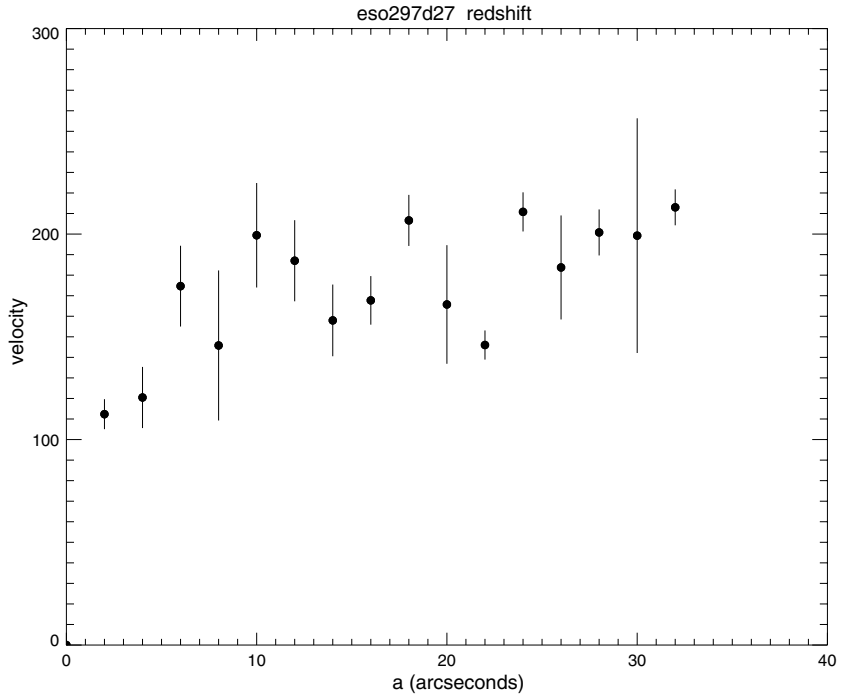

Figure 10. The rotation curve of ESO 297-27 folded and averaged from both sides of the galaxy. A line fitted to the disk of the profile gives $V_{max} = 204$ km s^{-1}. The fit implies a slight rise to the rotation curve. However, this result is based on the Hα disk, which appears to extend out to only 3/4 of the optical disk.

As an external check on our rotation data, we include in Figure 7 data points from the study of Mathewson et al. (1992). We graphically estimated Mathewson et al.'s velocities with an approximate error of 30 km s^{-1}. Each radius also had to be estimated and has an error of 1″. We defined the direction northwest of the galaxy's center, along the major axis, to be positive. We estimated the center of the galaxy as the pixel with the brightest continuum emission. This location corresponded to an Hα emission recessional velocity of 6365 ± 28 km s^{-1}. This value is in agreement with the Mathewson et al. (1992) value of 6362 ± 10 km s^{-1}. The deprojected rotation curve (Figure 8) appears normal and symmetric, but it does appear to rise slightly on one side. A folded and averaged velocity curve is seen in Figure 10. The averaged velocity curve still appears to rise

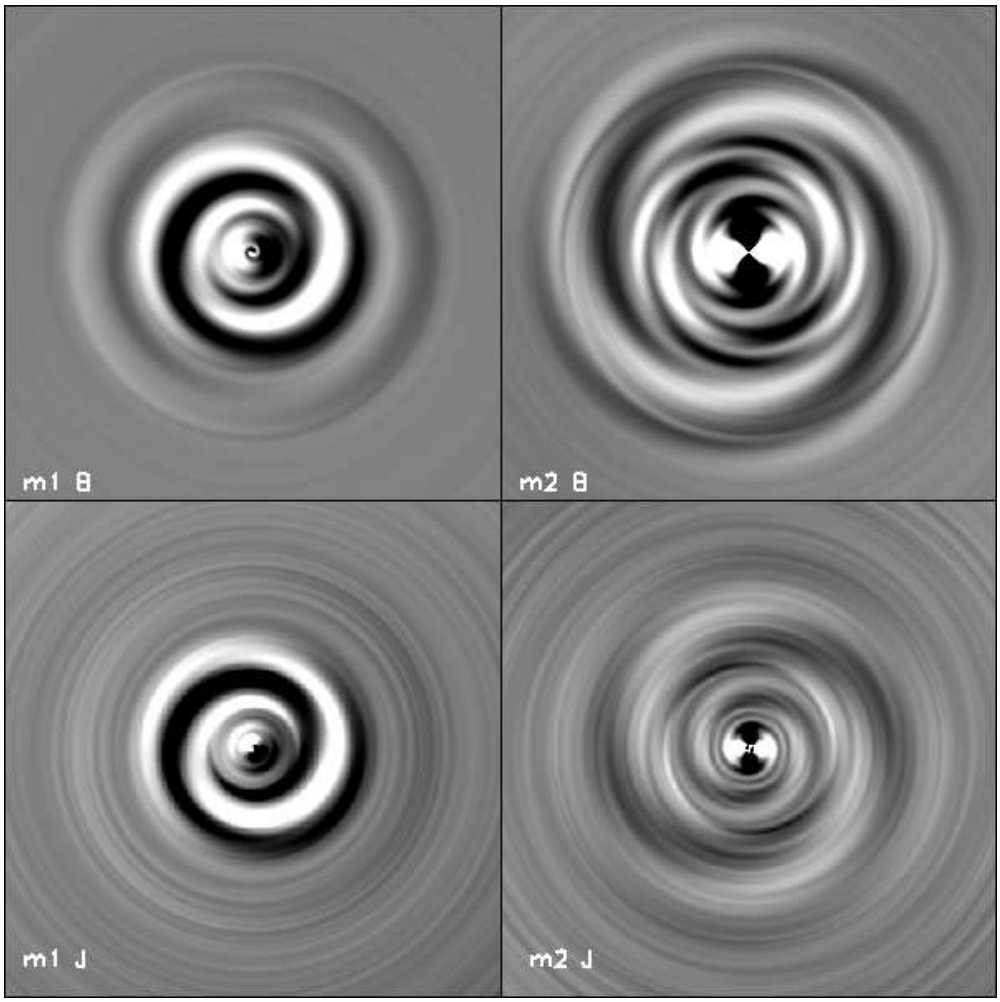

Figure 11. Deprojected images of ESO 297-27, showing the $m = 1$ Fourier component (left panels) and the $m = 2$ components (right panels).

slightly; however, the Hα disk was detected spectroscopically out to only 3/4 the radius of the optical disk. Therefore, the rotation curve may still flatten out at larger radii. Fitting a first-order polynomial to the outer disk of the galaxy gives a $V_{\rm max}$ estimate of 204 $\pm$ 15 km s^{-1}, which falls in between the average maximum velocities found by Rubin et al. (1985) for Sb (222 km s^{-1}) and Sc (174 km s^{-1}) galaxies (their Figure 7(c)).

4.2. Bulge-Disk Decomposition and Fourier Analysis

ESO 297-27 is an important example of a galaxy with a counter-winding structure. The galaxy has a single inner arm opening counterclockwise and three faint outer arms opening clockwise. The outer arms are barely visible above the background in the J-band image (see Figure 1). Although ESO 297-27 is not as strong a case as NGC 4622, it is still a useful case to study, especially since it lies in a much less dense environment than NGC 4622 (Buta et al. 1992).

We made the counter-winding structure less ambiguous and easier to see by decomposing the galaxy image into its Fourier components. This process required an image deprojected by using the mean axis ratio and position angle of the outer disk, assuming that these isophotes are intrinsically circular in shape (see Table 4). However, the bulge in this galaxy is less flattened than the disk, and this procedure stretched the isophotes of the bulge into elongated or "false bar" structure (Buta et al. 2007). In order to minimize this effect, we first decomposed the galaxy into its bulge and disk components.

To derive the bulge and disk parameters of ESO 297-27, we used the two-dimensional multi-component decomposition program described by Laurikainen et al. (2005, their Section 4.1). This program uses an exponential function to model disks and a Sérsic (1968) $r^{\frac{1}{n}}$ function to model bulges. It also allows for bars, lenses, and ovals. The program found no significant bar structure in ESO 297-27; therefore, the flux of the bar was forced to zero. We used the J-band image parameters to define the galaxy's bulge and disk shapes (see Table 5) because longer wavelength images are free of extinction and star-forming features. The optical-image-based parameters were consistent with the J-band disk profile but were less consistent with the J-band bulge profile possibly due to the effects of the inner arm. Table 5 lists the central surface brightnesses μ_{0b} and μ_{0d} and the radial scale lengths h_b and h_r for the J-band bulge and disk, respectively, and the Sérsic exponent $\beta = 1/n$, where n is the Sérsic index which is 1 for an exponential and 4 for the de Vaucouleurs $r^{\frac{1}{4}}$ law. Using the parameters derived for each filter, a modeled bulge was subtracted from the sky plane image. The remaining disk was then deprojected using the axial ratio of the outer isophotes found from the IRAF routine ELLIPSE. Once the disk was deprojected, the bulge was added back as a spherical component creating a deprojected view of the galaxy (upper left panel of Figure 12).

Table 5
Two-dimensional Decomposition Parameters of ESO 297-27

Parameter	J (NTT)
μ_{0b} (mag arcsec^{-2})	17.23
$R_{\rm eff}$ (arcsec)	2.01
β	0.80
μ_{0d} (mag arcsec^{-2})	20.28
h_r (arcsec)	12.43
B/T	0.10

Notes. Row 1: central surface brightness of the bulge. Row 2: effective radius o the bulge. Row 3: β is the exponent of the Sérsic law. Row 4: central surface brightness of the disk. Row 5: radial scale length of the disk. Row 6: major axis of the oval component fitted to the galaxy. Row 7: axis ratio of the oval component fitted to the galaxy. Row 8: fraction of bulge mass to total galaxy mass. Row 9: fraction of disk mass to total galaxy mass.

The decomposition results in a bulge model which contributes only 10% of the total luminosity and has a Sérsic n parameter of 1.24 in the J-band. This value of n suggests that ESO 297-27 has a *pseudo-bulge* rather than a classical bulge (Kormendy & Kennicutt 2004). Both the n and the B/T-values are typical for ESO 297-27's morphological type (Laurikainen et al. 2007, their Figure 3).

Having created a deprojected image of the galaxy, we then decomposed the galaxy into its Fourier components. This analysis was done by expanding the light distribution into a Fourier series,

$$I(r,\theta) = I_o(r) + \sum_{m=1}^{\infty} I_{mc}(r)\cos(m\theta) + \sum_{m=1}^{\infty} I_{ms}(r)\sin(m\theta), \quad (2)$$

where $I(r,\theta)$ is the observed deprojected light distribution, r is the radius from center, θ is the polar angle in the galaxy plane, $I_o(r)$ is the azimuthally averaged light distribution, $I_{mc}(r)$ and $I_{ms}(r)$ are the cosine and sine amplitudes, respectively, of azimuthal variations in surface brightness at a given radius, and m is an integer. The sine and cosine amplitudes are derived by taking moments of the light distribution (Buta 1986). With these amplitudes, we reconstructed images of the $m\theta$ components of the light distribution, as done for NGC 4622 by Buta et al. (1992, 2003).

In general, the $m = 1$ Fourier component shows the first-order asymmetry of a galaxy, such as in alternating arcs and one-armed spirals. The $m = 2$ image shows the large-scale symmetric features such as two-armed spirals and ovals. The left panels of

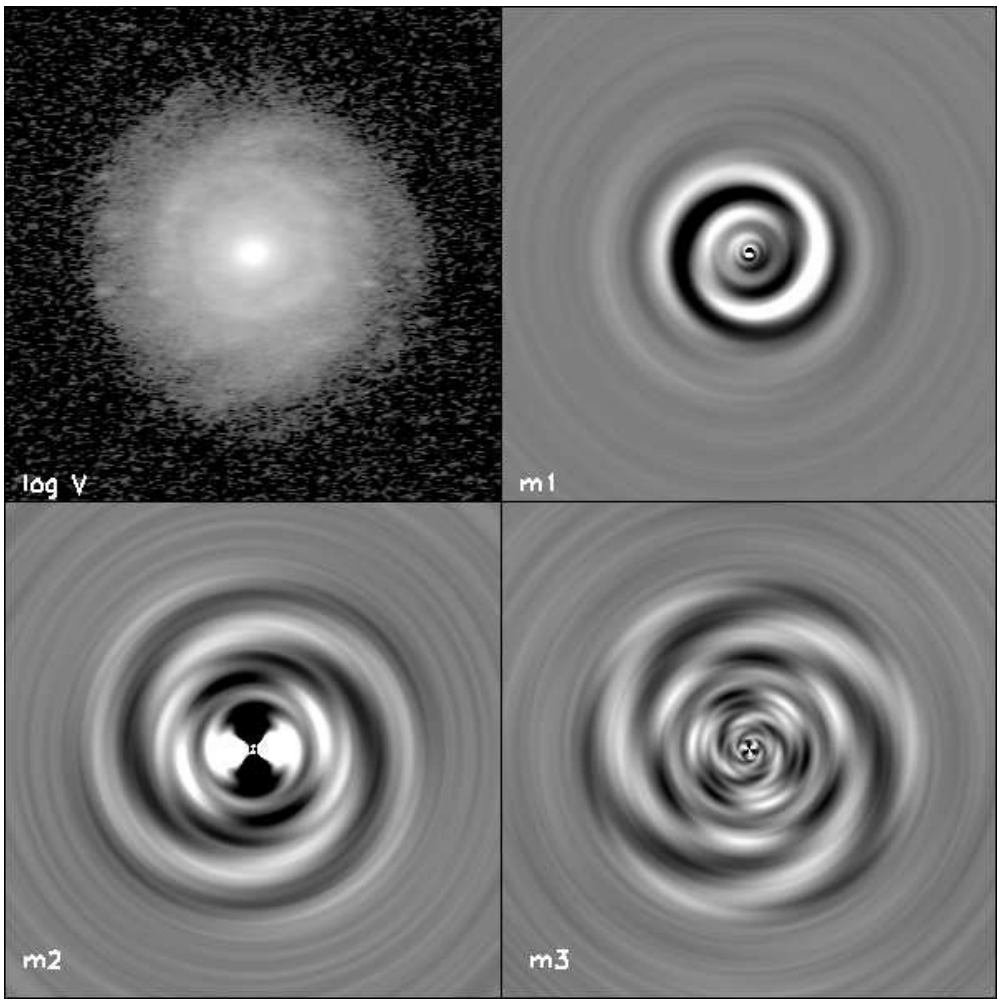

Figure 12. A set of Fourier images of ESO 297-27, based on the V-band CTIO image. The upper left panel shows the total image, while the other panels show the $m = 1$, 2, and 3 components as indicated.

Figure 11 show the $m = 1$ component in the B and J bands, while the right panels show the $m = 2$ components. These images were based only on the ESO NTT data. Figure 12 shows the $m = 1$, $m = 2$, and $m = 3$ Fourier components of the CTIO V-band image. As expected, ESO 297-27 has a strong $m = 1$ component in all filters, representing the single inner arm. The Fourier image smooths over much of the apparent irregularity of this arm seen in blue light. The outer arms, seen mainly in the higher-order images, clearly open in the opposite sense to the inner arm. Although the outer pattern is weakly three-armed as seen in the $m = 3$ component, the Fourier analysis still detects an $m = 2$ component. The amplitude of this component mostly models the transition between the inner and the outer spiral structures. However, the decomposition left a residual oval in the center of the galaxy that has some $m = 2$ amplitude due to our assumption that the bulge is intrinsically spherical. The Fourier analysis suggests that the counter-winding spiral structure of ESO 297-27 is real and not a chance phenomenon due to viewing angle or the discrete placement of dust or star formation.

4.3. Leading Versus Trailing Spiral Structure

4.3.1. The Near Side of the Disk

We demonstrated that ESO 297-27 has a rare counter-winding spiral structure arranged in a manner very similar to NGC 4622: a single inner arm counter-winding relative to two or more outer arms. Unless the galaxy also has *counter-rotating* components (see Section 5), one set of arms must be leading while the other set is trailing. Since we have no evidence supporting a counter-rotating disk, we proceed with the assumption that one set of spiral arms is leading.

With our images and rotation data, we are in a position to apply the dust asymmetry method to ESO 297-27. The advantage we have with this galaxy over NGC 4622 is an inclination high enough, and a Hubble-type late enough, to allow us to detect a dust asymmetry in our ground-based ESO-NTT images. The much lower inclination of NGC 4622 made ground-based images of average seeing incapable of determining which spiral pattern is leading.

While a late-type spiral has the advantage of a dustier disk to accent the tilt of the galaxy, it also has a disadvantage of a smaller bulge that will highlight the dust less. Originally, the de Vaucouleurs' tilt asymmetry method was intended for bulge-dominated disk galaxies. However, the effect should work with any sized spherical or oblate spheroidal galaxy component. ESO 297-27 has a B/T ratio of only 0.05 (see Section 4.2). Even though the bulge is relatively small, we would expect to see a dust asymmetry within the innermost region of ESO 297-27.

The $B - J$ color index maps in Figure 1 suggest that the north side of the galaxy is the near side. On the north side of the minor axis, significant reddening is seen within 10″ of the center in a manner which is typical of near-side extinction. This is quantified in Figure 13 using surface brightness and color difference profiles along the minor axis. These show that, within 10″ from the center, the surface brightness on the north side is not only fainter than that on the south side, but also redder in color. If we assume that the galaxy's color and surface brightness are intrinsically symmetric across the minor axis, then any difference in color and brightness must be due to internal extinction. The $m = 1$ single arm component may affect the color and surface brightness comparison between the

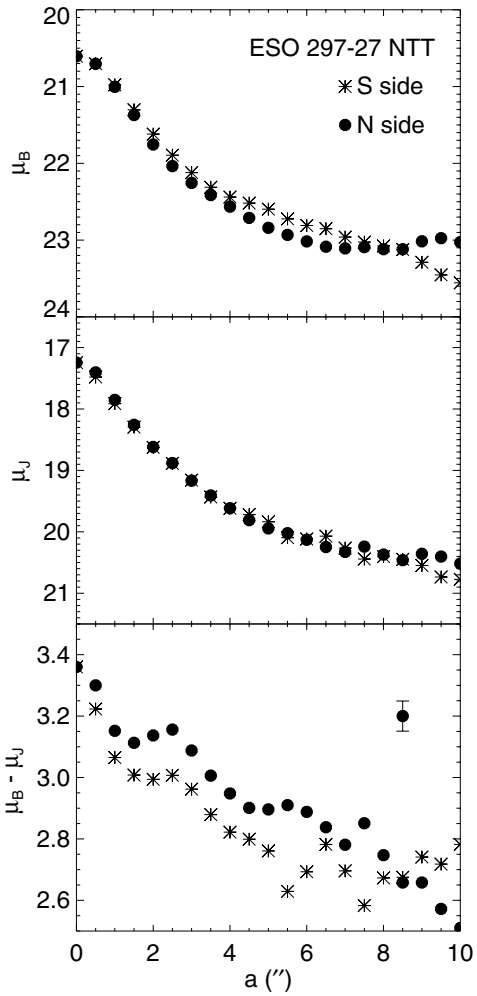

Figure 13. Surface brightness and color index profiles along the minor axis of ESO 297-27. These panels show that the north side is both fainter and redder than the south side, suggesting that the north side is the near side. The bottom panel has a representative error of $\delta(B - V) = 0.049$ mag. The top and middle panels have errors of $\delta B = 0.030$ mag and $\delta J = 0.039$ mag, respectively. These errors are smaller than the point sizes and, therefore, were not plotted.

northern and southern sides. However, due to the small bulge, we focused our comparison on the inner 10″ of the galaxy where the $m = 1$ component is less prominent and would have a smaller effect on altering the galaxy's color and brightness.

It is possible that the observed dust asymmetry in ESO 297-27 is intrinsic to the galaxy. Late-type spirals tend to be more asymmetric than earlier types, so it is easy to assume that the dust distribution would also be asymmetric. If this is the case, it is highly improbable that the dust asymmetry would align with the minor axis of the galaxy. Since the asymmetry would be real and therefore random, so should its placement within the galaxy. In ESO 297-27 the dust asymmetry appears to be aligned with the minor axis of the galaxy as seen in Figure 1, which leads us to believe that this asymmetry is due to orientation and is not intrinsic to the galaxy.

This is further verified by the plot in Figure 14, which shows the color difference $\delta(B - J) = (\mu_B - \mu_J)(\text{north}) - (\mu_B - \mu_J)(\text{south})$ versus the surface brightness difference $\delta B = \mu_B(\text{north}) - \mu_B(\text{south})$ within 10″ radius along the galaxy minor axis (position angle 171°). Almost all of these points are in the upper right quadrant of the plot. The line shown is based on the relative extinction value of Cardelli et al. (1989, their Table 3),

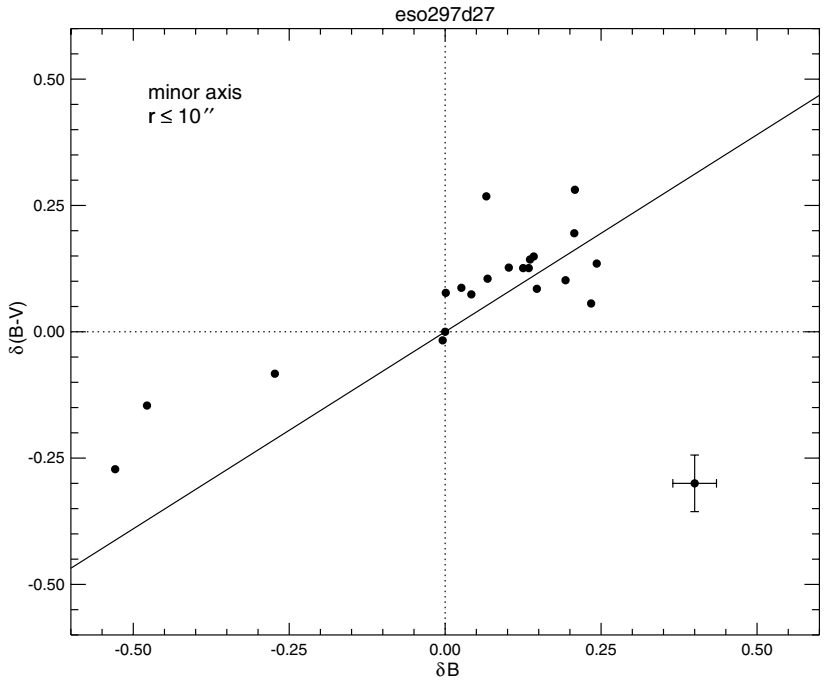

Figure 14. Plot of $\delta(B-J) = [(\mu_B - \mu_J)(\text{north}) - (\mu_B - \mu_J)(\text{south})]$ vs. $\delta B = \mu_B(\text{north}) - \mu_B(\text{south})$. Representative errors in δB and $\delta(B-V)$ are 0.035 mag and 0.056 mag, respectively. The line is based on the extinction vs. wavelength values from Cardelli et al. (1989).

Table 6
Nearby Companions of ESO 297-27[a]

Name	R.A. (J2000)	Decl. (J2000)	Type	Redshift (z)	D_{maj} (arcmin)	D_{min} (arcmin)	J_{TOTAL}	b_J
LEDA 097503[b]	01:44:25.2	−41:49:55	(R_1')SB(s)ab H II	0.02034	0.63	0.57	12.414	15.07
ESO 297-26	01:44:59.3	−41:59:36	Sbc	0.03383	1.04	0.16	12.796	16.10
ESO 297-27	01:45:10.8	−41:52:48	SA(rs)ab	0.02122	1.3	0.7	12.849	15.08
ESO 297-28	01:45:44.1	−41:57:22	S	0.02890	1.0	0.2	...	16.01

Notes.
[a] All data in the table were taken from the online NED.
[b] Also known as 2MASS J01442525-4149546.

which gives $\delta(B-J) = 0.78\delta B$. If the apparent correlation between $\delta(B-J)$ and δB is due to extinction, and if the dust largely acts like a "screen," then the Cardelli et al. relation should be approximately valid. Within the large scatter this appears to be the case. Again, we conclude that the reddening on the north side is due to internal extinction, and that it reliably tells us the near side of the galaxy.

4.3.2. Approaching and Receding Halves of the Disk

The rotation curve of ESO 297-27 is well defined from Hα and [N II] emission in our spectra. Figure 8 shows that the rotation profile is flat on both sides of the major axis and looks relatively normal. From the profile, we establish that the northeast side of the galaxy is receding and the southwest side is approaching relative to the galaxy center. In the previous section, we determined that the north side of the galaxy is also the near side. Putting these two facts together, we conclude that the galaxy rotates counterclockwise. As a consequence of the rotation, *the three outer arms are trailing spirals while the single inner arm is a leading spiral.*

The results for ESO 297-27 stand in contrast to NGC 4622, which has a single trailing inner arm and two strong leading outer arms. In both cases, however, the strongest spiral pattern is found to have the leading sense. Also, the sense of winding in both cases was determined by the dust asymmetry method. Morphologically, ESO 297-27 is a more normal-looking spiral than NGC 4622. The latter is significantly lop-sided, while the former is much less so. Another significant difference between NGC 4622 and ESO 297-27 is that in NGC 4622, the single counter-winding arm is largely stellar in nature, while in ESO 297-27, all the spiral arms have a significant gaseous component.

4.4. Possible Causes of Odd Morphology

An NED search for objects near ESO 297-27 results in three significant neighbors. These are listed in Table 6. Two candidates, ESO 297-26 and ESO 297-28, have radial velocities more than 2000 km s^{-1} higher than ESO 297-27's velocity of 6362 km s^{-1}, and are likely to be background objects. The third companion, 2MASX J01442525-4149546 (LEDA 097503 for short in Table 6), has a velocity of 6099 km s^{-1}, is 9.′0 from ESO 297-27, and is likely to be physically related to ESO 297-27. Their apparent separation corresponds to about 220 kpc in projected separation.

We also studied our new images for any uncatalogued, closer companions. A small galaxy lies 46″ to the northeast of the center of ESO 297-27 (see Figure 1). Simulations show that small companions ($M_{\text{comp}} = 0.01 M_{\text{Disk}}$) approaching within

0.1 $R_{\rm Disk}$ create a leading spiral structure that lasts for a billion years (Byrd et al. 1993). It is possible that this galaxy affected ESO 297-27's morphology in the recent past; however, there is no way to confirm this without velocity data for this galaxy.

5. DISCUSSION

Galaxies like ESO 297-27 and NGC 4622 pose a dilemma for spiral structure theories because of the difficulty of maintaining leading spirals. The maintenance of spirals is thought to depend on an outward transport of angular momentum, and only trailing spirals can do this effectively (Lin & Lau 1979). Angular momentum may propagate outward through an exchange with the outer Lindblad resonance, gas dissipation, or an interaction with the galaxy's halo. However, Lin & Lau (1979) argue that the angular momentum of long wave leading spirals, the only kind that have an outward group velocity beyond corotation, is not easily absorbed. This makes it difficult for a stellar disk to maintain a conspicuous leading spiral.

The presence of a counter-winding spiral pattern within a galaxy does not conclusively mean that the galaxy has a leading spiral structure. There is a real possibility that the two sets of spiral arms exist in counter-rotating disks. Currently we have no evidence, either for ESO 297-27 or for NGC 4622, that counter-rotation is at the heart of counter-winding spirals. If the domains of the patterns are dominated by counter-rotating stars, then conceivably *both* patterns could be trailing. Each spiral would then be able to transfer angular momentum outward and maintain itself. However, it is unclear whether such an arrangement could last very long.

We highlight two cases that suggest to us that counter-rotation in a disk galaxy does not necessarily lead to counter-winding spirals. NGC 4138 and NGC 7742 are two examples of nonbarred ringed galaxies where counter-rotation has been detected. NGC 4138 (type SA(r)a; Buta et al. 2007) was discovered by Jore et al. (1996) to have a disk of ionized and atomic gas, as well as stars, rotating counter to a primary disk comprised of 80% of the galaxy's stars. Jore et al. consider that the origin of the counter-rotating material is either a dwarf galaxy merger or gas accretion from an outside reservoir. They state that counter-rotating material is found throughout the galaxy, but peaks around the radius of the galaxy's inner ring. NGC 7742 (type S$\underline{\rm A}$B(r)ab; Buta et al. 2007) is a nearly face-on early-type spiral showing a bright inner ring made of tightly wrapped spiral structure. de Zeeuw et al. (2002) found that the ionized gas in the inner ring counter-rotates with respect to the stars inside the ring. Fourier analysis of an *HST* archival *B*-band image of NGC 7742 confirms that the tightly wrapped ring spiral and the much fainter outer arms wind outward in the same sense. According to de Zeeuw et al. (2002), all of the spiral arms in NGC 7742 would be trailing if its northeast side is the near side. The lack of counter-winding spirals in NGC 7742 suggests that all the spiral structure seen in the galaxy is associated with the counter-rotating gas disk.

In both of these cases, it is likely that external gas or a small companion has been accreted and settled into a counter-rotating disk that is mostly coplanar with a pre-existing disk. Counter-winding spiral structure is not evident in either case. Gas accretion or minor mergers do not necessarily lead to counter-winding spirals. This suggests either that an external interaction, such as a small (nonmerging) companion, or some internal mechanism could be responsible for counter-winding arms.

Zhang & Buta (2007) have suggested that the counter-winding spirals in NGC 4622 are transient density *waves* and not density wave *modes*. Naturally excited modes are expected to be long-lived (Bertin et al. 1989a, 1989b), but waves only last as long as their generating mechanism allows. If the patterns we see in ESO 297-27 and NGC 4622 are only density waves, this could explain the extreme rarity of such systems.

6. CONCLUSIONS

We have presented optical and spectroscopic data on ESO 297-27, a normal looking intermediate-to-late-type spiral galaxy. With these data, we calculated and updated the physical parameters of ESO 297-27. We found the galaxy to have an Hα luminosity of 2.58×10^{41} erg s^{-1}. This rate of Hα emission converts into a star-formation rate of 2.0 $M_{\odot}$ yr^{-1} which is typical for intermediate-to-late-type spirals (KTC). The galaxy is tilted approximately 58°, making it possible for us to determine its near side. We did this by measuring the dust asymmetry across its minor axis, and we found the northern edge of the galaxy to be the near side. This reddening effect can also be seen in the color index map shown in Figure 1. We derived a velocity curve from the galaxy's Hα and [N II] emission. The velocity data agree well with previous data obtained by Mathewson et al. (1992) and give a systemic velocity of 6365 ± 28 km s^{-1}. Fitting a line to the outer disk velocities, we estimated the maximum velocity of the observed H II disk to be $V_{\rm max} = 204 \pm 15$ km s^{-1}. The major axis rotation profile shows that the southwestern edge of the galaxy moves toward us. Closer study of its morphology showed ESO 297-27 to have a counter-winding spiral structure. The features are subtle, but distinguishable even on SRC-J sky survey charts. Our Fourier analysis strengthens this conclusion. We show that the inner single arm of ESO 297-27 is leading and the three outer arms are trailing. This result is in contrast with NGC 4622, which lies in a denser environment.

This project has been supported by NSF grant AST 050-7140 to the University of Alabama. This research has made use of the NASA/IPAC Extragalactic Database (NED), which is operated by the Jet Propulsion Laboratory, California Institute of Technology, under contract with NASA. We thank the anonymous referee and William Keel for their helpful comments. We also thank NOAO, CTIO, and ESO for use of the 1.5 m, 0.9 m, 3.6 m, and 4.0 m telescopes. Observations with the ESO NTT were supported by the Academy of Finland.

REFERENCES

Bertin, G., Lin, C. C., Lowe, S. A., & Thurstans, R. P. 1989a, ApJ, 338, 78
Bertin, G., Lin, C. C., Lowe, S. A., & Thurstans, R. P. 1989b, ApJ, 338, 104
Binney, J., & Tremaine, S. 1987, Galactic Dynamics (Princeton, NJ: Princeton Univ. Press)
Buta, R. 1986, ApJS, 61, 631
Buta, R. 1995, ApJS, 96, 39
Buta, R., Byrd, G., & Freeman, T. 2003, ApJ, 125, 634
Buta, R., & Combes, F. 1996, Fund. Cosmic Phys., 17, 95
Buta, R., Corwin, H. G., & Odewahn, S. C. 2007, The de Vaucouleurs Atlas of Galaxies (Cambridge: Cambridge Univ. Press)
Buta, R., Crocker, D. A., & Byrd, G. G. 1992, AJ, 103, 1526
Byrd, G. G., Freeman, T., & Howard, S. 1993, AJ, 105, 477
Byrd, G. G., et al. 1989, Cel. Mech., 45, 31
Cardelli, J. A., Clayton, G. C., & Mathis, J. S. 1989, ApJ, 345, 245
Crocker, D. A., Baugus, P. D., & Buta, R. 1996, ApJS, 105, 353
de Vaucouleurs, G. 1958, ApJ, 127, 487
de Vaucouleurs, G. 1959, HDP, 53, 275
de Vaucouleurs, G., et al. 1991, Third Reference Catalog of Bright Galaxies (New York: Springer) (RC3)
de Zeeuw, P. T., et al. 2002, MNRAS, 329, 513

Graham, J. A. 1982, PASP, 94, 244
Grouchy, R., & Buta, R. 2005, BAAS, 206, 1006
Howarth, I. D. 1983, MNRAS, 203, 301
Hubble, E. 1943, ApJ, 97, 112
Jacoby, G. H., Quigley, R. J., & Africano, J. L. 1987, PASP, 99, 672
Jore, K. P., Broeils, A. H., & Haynes, M. P. 1996, AJ, 112, 438
Joyce, R. R. 1992, in ASP Conf. Series 23, Astronomical CCD Observing and Reduction Techniques, ed. S. B. Howell (San Francisco, CA: ASP), 258
Keel, W. C. 1996, ApJS, 106, 27
Kennicutt, R. C. 1983, ApJ, 272, 54
Kennicutt, R. C., Tamblyn, P., & Congdon, C. W. 1994, ApJ, 435, 22 (KTC)
Kohoutek, L., & Martin, W. 1981, A&AS, 44, 325
Kormendy, J., & Kennicutt, R. C. 2004, ARAA, 42, 603
Landolt, A. 1973, AJ, 78, 959
Landolt, A. 1983, AJ, 88, 439
Laubert, A., & Valentijn, E. A. 1989, The Surface Photometry Catalogue of the ESO-Uppsala Galaxies (Garching: European Southern Observatory)
Laurikainen, E., Salo, H., & Buta, R. 2005, MNRAS, 362, 1319
Laurikainen, E., Salo, H., Buta, R., & Knapen, J. H. 2007, MNRAS, 381, 401
Lin, C. C., & Lau, Y. Y. 1979, Stud. Appl. Math., 60, 97
Lin, C. C., & Shu, F. H. 1964, ApJL, 140, 646
Lynden-Bell, D., & Kalnajs, A. J. 1972, MNRAS, 157, 1
Mathewson, D. S., Ford, V. L., & Buchhorn, M. 1992, ApJS, 81, 413
Pasha, I. I. 1984, SvAL, 11, 1
Pasha, I. I., & Smirnov, M. A. 1982, Ap&SS, 86, 215
Rubin, V. C., Burstein, D., Ford, W. K., & Thonnard, N. 1985, ApJ, 289, 81
Rubin, V. C., Kenney, J. D. P., & Young, J. S. 1997, AJ, 113, 125
Sandage, A. 1961, The Hubble Atlas of Galaxies (Washington, DC: Carnegie Institution)
Schwarz, M. P. 1981, ApJ, 247, 77
Seaton, M. J. 1979, MNRAS, 187, 73
Sérsic, J. L. 1968, Atlas de Galaxies Australes (Cordoba: Universidad Nacional de Cordoba)
Sharp, N. A., & Keel, W. C. 1985, AJ, 90, 469
Shu, F. 1982, The Physical Universe (Mill Valley, CA: Univ. Science Books), 274
Toomre, A. 1981, Seng. Conf., 11, 1
van der Kruit, P. C., & Searle, L. 1981, A&A, 95, 105
Zhang, X., & Buta, R. 2007, AJ, 133, 2584